Microphysical properties of cold frontal rainbands

Crosier, J., Choularton, T. W., Westbrook, C. D., Blyth, A. M., Bower, K. N., Connolly, P. J., Dearden, C., Gallagher, M. W., Cui, Z. and Nicol, J. C. (2014) Microphysical properties of cold frontal rainbands. Quarterly Journal of the Royal Meteorological Society, 140 (681). pp. 1257-1268. ISSN 1477-870X doi: https://doi.org/10.1002/qj.2206 Available at http://centaur.reading.ac.uk/40875/

RMetS
Royal Meteorological Society

Microphysical properties of cold frontal rainbands†

J. Crosier[a,b,*] T. W. Choularton[b], C. D. Westbrook[c], A. M. Blyth[d,e], K. N. Bower[b], P. J. Connolly[b], C. Dearden[b], M. W. Gallagher[b], Z. Cui[e] and J. C. Nicol[f,c]

[a]*National Centre for Atmospheric Science, University of Manchester, UK*
[b]*Centre for Atmospheric Science, University of Manchester, UK*
[c]*Department of Meteorology, University of Reading, UK*
[d]*National Centre for Atmospheric Science, University of Leeds, UK*
[e]*School of Earth and Environment, University of Leeds, UK*
[f]*National Centre for Atmospheric Science, University of Reading, UK*

*Correspondence to: J. Crosier, School of Earth, Atmospheric and Environmental Sciences, University of Manchester, Oxford Rd, Brunswick Street, Manchester M13 9PL, UK. E-mail: j.crosier@manchester.ac.uk

Observations have been obtained within an intense (precipitation rates > 50 mm h^{-1}) narrow cold-frontal rainband (NCFR) embedded within a broader region of stratiform precipitation. *In situ* data were obtained from an aircraft which flew near a steerable dual-polarisation Doppler radar. The observations were obtained to characterise the microphysical properties of cold frontal clouds, with an emphasis on ice and precipitation formation and development.

Primary ice nucleation near cloud top (-55°C) appeared to be enhanced by convective features. However, ice multiplication led to the largest ice particle number concentrations being observed at relatively high temperatures ($> -10^{\circ}$C). The multiplication process (most likely rime splintering) occurs when stratiform precipitation interacts with supercooled water generated in the NCFR. Graupel was notably absent in the data obtained.

Ice multiplication processes are known to have a strong impact in glaciating isolated convective clouds, but have rarely been studied within larger organised convective systems such as NCFRs. Secondary ice particles will impact on precipitation formation and cloud dynamics due to their relatively small size and high number density. Further modelling studies are required to quantify the effects of rime splintering on precipitation and dynamics in frontal rainbands. Available parametrizations used to diagnose the particle size distributions do not account for the influence of ice multiplication. This deficiency in parametrizations is likely to be important in some cases for modelling the evolution of cloud systems and the precipitation formation. Ice multiplication has significant impact on artefact removal from *in situ* particle imaging probes.

Key Words: ice multiplication; cold front; rainband; radar; *in situ* microphysics; precipitation

Received 9 November 2012; Revised 1 May 2013; Accepted 27 May 2013; Published online in Wiley Online Library 30 September 2013

1. Introduction

Mature midlatitude cyclones often have one or more distinct precipitation features associated with them. The location of the features with respect to the moving frontal system, as well as the intensity of precipitation, is indicative of the processes that form them. A summary of the precipitation features (referred to as rainbands, due to their banded structure) associated with midlatitude cyclones was given by Matejka *et al.*(1980), who introduced the concept of two types of rainband associated with cold frontal passage: Narrow and Wide Cold Frontal Rainbands (referred to as NCFR and WCFR respectively).

The NCFR is a region of heavy precipitation typically orientated along the surface cold front. Precipitation in the NCFR is formed due to intense line convection generated near the surface, where rearward sloping cold air undercuts and lifts the moist warm sector air approaching the surface cold front, in a system-relative sense (Browning, 1986). NCFRs can be over 100 km in length along the surface cold front, but are only a few kilometres in width,

† [The copyright line in this article was changed on 30 May 2014 after original online publication.]

and can generate precipitation rates as high as 100 mm h^{-1}. These high precipitation rates are observed at the surface for only a few minutes as the system passes overhead. Passage of a NCFR also results in sudden drops in temperature/wind speed, a veer in the wind direction, and a jump in pressure at the surface (James and Browning, 1979). Browning and Reynolds (1994) highlight an additional mechanism for NCFR generation, via the downward transport of stratospheric air, leading to strong surface gusts which initiate convection.

The line of intense precipitation associated with a NCFR is frequently broken into smaller elements (referred to as precipitation cores) separated by a quiescent region of suppressed precipitation called a gap region (James and Browning, 1979; Hobbs and Persson, 1982; Browning and Roberts, 1996). The smaller bands of heavy precipitation range in size from a few kilometres to tens of kilometres in length, while still remaining a few kilometres wide. The gap regions can be of a similar size to the precipitation cores, but are typically smaller (Locatelli *et al.*, 1995). Locatelli *et al.*(1995) and Jorgensen *et al.*(2003) discuss the positive feedback between convection and precipitation: the effect of cooling in the cold sector by evaporation/melting of precipitation leads to enhanced baraclinicity, and strengthens cold-air advection and thus convection.

The WCFR is a region of light precipitation which spans the front over a greater horizontal extent (several tens of kilometres), along the length of the surface cold front (Matejka *et al.*, 1980). It results from the gradual slantwise ascent at mid/upper levels which occurs during frontal passage. The position of the NCFR with respect to the WCFR, and the formation of gap regions in the NCFR are largely determined by the position of the upper-level cold front relative to the surface cold front (Browning, 1986; Browning and Roberts, 1996). This is itself determined by the progression of the dry intrusion around the trough and into the cloudy warm conveyor belt region.

The CYCLES project (Matejka *et al.*, 1980) and IMPROVE (Stoelinga *et al.*, 2003) field campaigns examined the roles of dynamics and microphysics in rainbands associated with frontal systems through a combination of airborne *in situ* microphysics, Doppler radar, radiosondes and surface observations. For example, Rutledge and Hobbs (1984) concluded that efficient graupel production (facilitated by liquid water generation due to rapid ascent at the surface cold front) was responsible for the majority of the precipitation in the NCFR. They also observed high ice particle number concentrations in this same region (attributed to rime splintering; Hallett and Mossop, 1974), but these ice particles did not contribute significantly to the precipitation.

As has just been discussed, the precipitation and dynamical structure of NCFRs has been investigated by several studies over the past three decades. However, there have been relatively few studies which have examined the cloud microphysical properties of such systems in detail. Those which have are likely affected by artefacts which were unknown/uncorrected at the time. In this article we present airborne *in situ* microphysics, surface observations and dual polarisation Doppler radar measurements from cloud associated with a cold front that has a NCFR embedded within a WCFR. The measurements presented are obtained using the most up-to-date probes at the time, and processed to eliminate potential artefacts which have only recently been identified (Field *et al.*, 2006; Korolev *et al.*, 2011). Our results are compared qualitatively with those from the previous studies which may have been affected by these artefacts.

2. Methodology

Measurements of cloud microphysical properties were collected in mixed-phase clouds in the UK during 2007–2010 as part of the NERC-funded Aerosol Properties, PRocesses And InfluenceS on the Earth's climate (APPRAISE) programme, Clouds project (APPRAISE-Clouds). *In situ* measurements were collected on board the UK Facility for Airborne Atmospheric Measurement (FAAM) BAe-146 aircraft. Remote-sensing measurements were also performed at the Chilbolton Facility for Atmospheric and Radio Research (CFARR) in southern England (51.14°N, 1.44°W). Objectives of APPRAISE-Clouds focus on the impact of aerosols on cloud microphysical properties (Crosier *et al.*, 2011; Westbrook and Illingworth, 2011; Crawford *et al.*, 2012; Cui *et al.*, 2012). We present measurements collected on 3 March 2009, in cloud associated with a cold frontal system which passed over CFARR at approximately 2035 UTC. A summary of the instrumentation used can be found below. Additional information on instrumentation can be found in Crosier *et al.* (2011).

In situ microphysical measurements on board the BAe-146 were obtained from a cloud droplet probe (CDP; Lance *et al.*, 2010), cloud imaging probes CIP-15 and CIP-100 (Baumgardner *et al.*, 2001) and a two-dimensional stereo probe (2D-S; Lawson *et al.*, 2006). Particle Inter-Arrival Time (IAT) filtering was applied to remove shattering artefacts (Field *et al.*, 2006) from the CIP-15 and CIP-100 data. Details of the IAT thresholds used are described later. Anti-shatter tips to prevent sampling artefacts (as described by Korolev *et al.*, 2011) were not fitted for this study. The CIP-15 and CIP-100 data were also merged to create a synthesised size distribution from $\sim$ 60 to 6200 μm. The changeover between the 15 and 100 μm resolution probe occurred at $\sim$ 550 μm and was decided upon by considering both sample volume and image resolution. Particle size (D_p) is defined as the average of the maximum size in the along- (D_y) and across- (D_x) array directions. Note this differs from the commonly used D_x size, which is sensitive to orientation for elongated particles. The sizing metric we use exhibits weaker sensitivity (approximately by a factor of 2) to particle orientation, which is important when trying to capture the true size distribution in areas dominated by elongated particles such as those which we highlight in this article. We have used the 'all-in' sample volume approach (Heymsfield and Parrish, 1978) and so reject partially imaged particles. The 2D-S is used in this article to provide higher-resolution (10 μm pixel) images of the measured particles. It was not used in the size distributions as it suffered from technical problems at high altitude ($T < -38$°C). *In situ* observations of vertical air motions were not obtained due to the five-hole turbulence probe (mounted on the aircraft nose radome) experiencing technical problems in the icing conditions.

Remote sensing of precipitation-sized particles was performed using the Chilbolton Advanced Meteorological Radar (CAMRa; Goddard *et al.*, 1994), a steerable 3 GHz dual-polarisation Doppler radar with a narrow 0.28° beam. The BAe-146 aircraft was able to operate only along the 255° (westsouthwest) radial because of air-traffic control restrictions, therefore RHI (range–height indicator) scans were made by CAMRa continuously along this radial.

Vertical air motion may be estimated using Doppler velocity measurements from RHIs by assuming mass-weighted flow continuity (e.g. Chapman and Browning, 1998). At low elevation angles (less than about 10°), the Doppler velocity is approximately equal to the radial component of the horizontal wind as the influence of vertical air motion and the vertical fall speeds of the targets (e.g. rain) may be neglected. Vertical air velocities (w) may then be estimated by integrating the observed convergence of the radial wind throughout each column assuming the boundary condition $w = 0$ at some height and taking density changes with height into account. We have chosen to integrate downwards, assuming that $w = 0$ at the echo top, as the radar is unable to sample sufficiently close to the surface except at very close ranges. Errors related to this assumption will exist throughout each column, however it is likely that vertical motions at the echo top will be significantly weaker than in the updraught near the surface at the frontal boundary and so can largely be neglected. This technique also requires that there is negligible divergence into the plane of the RHI; based on the linear structure of the NCFR, we shall assume that this is true.

3. Results and discussion

A cold frontal system passed over the UK on 3 March 2009, arriving at the west coast at ~1800 UTC. Widespread precipitation was associated with the passage of this front, in the form of a WCFR with low/moderate intensity of precipitation ($P < 10$ mm h^{-1}). A NCFR of much higher precipitation intensity ($P > 50$ mm h^{-1}) was also present and (as is characteristic of such rainbands) only affected a narrow region along the surface cold front. In the following paragraphs the synoptic situation and the rainband structure will be described. We then shift emphasis onto the microphysics of the rainband.

3.1. Synoptic overview

Figure 1 presents an overview of the synoptic situation at 1800 UTC using ECMWF operational analysis data (0.25° resolution). Data shown in Figure 1(a) are mean sea level pressure contours and equivalent potential temperature at 500 hPa. The location of the CFARR ground site is marked as a black cross. A trough located between the UK and Iceland was associated with the advection of cold air to the southeast, where it intercepted a tongue of warmer air. The warmer air flowed to the north at the eastern side of the trough in the form of a warm conveyor belt (Browning, 1986). Kinks in the sea-level isobars over Ireland/Celtic Sea (coincident with the region of rapidly changing equivalent potential temperature, θ_e), indicate the presence of a cold front.

Vertical cross-sections (along 51.24°N latitude) of θ_e and relative humidity fields are shown in Figure 1(b) and (c), respectively. The θ_e cross-section (Figure 1(b)) highlights the cold sector found to the west of the trough (CS1) and the warm sector (WS) adjacent to this on the eastern side of the front. The boundary between these represents the cold frontal surface (Browning, 1986). To the east of the warm sector, another cold sector (CS2) is visible. The transition between the WS and CS2 represents the warm front associated with the cyclone. This is not the focus of this article but is mentioned to identify all the features found within the figure. The relative humidity field (Figure 1(c)) shows a region of dry air above CS1. This suggests that overrunning of the cloudy warm conveyor air by the dry intrusion has occurred at this location, which fits the description of a kata-type cold front (Browning and Roberts, 1996). However, the rearward-sloping ascent/line convection observed is an ana-type characteristic (Agusti-Panareda *et al.*, 2009), so this case is some form of hybrid of the two types. The WS is characterized by high relative humidity due to the mesoscale ascent.

The corresponding infrared satellite image (1800 UTC from Meteosat Second Generation, MSG) is shown in Figure 2. A large continuous band of cloud associated with ascent in the warm conveyor belt is located over the Celtic Sea, Bay of Biscay and mainland UK. Cloud-top temperatures in the warm sector frontal clouds were of the order of −50°C according to both the ECMWF analysis data and from the multi-channel MSG retrieval (albeit with significant variations of approx ±10°C using the latter). To the northwest of this frontal cloud, the cold sector has a more broken cloud field, some parts of which have significantly higher cloud-top temperatures (around −10°C). There is possible evidence for the erosion of upper-level clouds by the dry intrusion occurring over the Irish Sea.

3.2. Rainband structure

The precipitation structure for the frontal system of interest is shown in Figure 3 using data from the UK Met Office operational radar network (NIMROD). Data are shown for three times, 1800, 1900 and 2000 UTC, to show the temporal evolution. Figure 3(a)–(c) show a region of moderate precipitation (1–10 mm h^{-1}) which follows the approximate location of the cold front as inferred from the infrared satellite image (Figure 2) and ECMWF analysis (Figure 1). This precipitation band is typically 100 km wide, and is either a WCFR or a warm-sector rainband (but most likely a combination of the two). Regions of high precipitation rate are also observed but are not easily visible due to their small size.

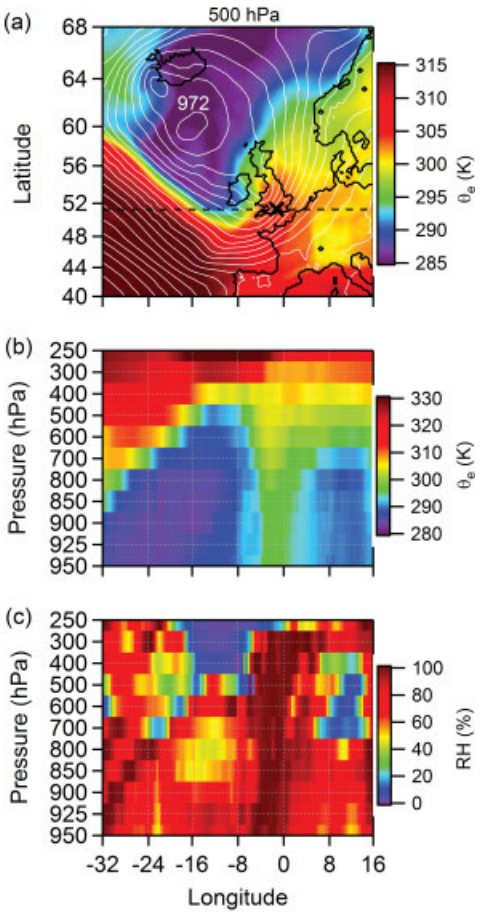

Figure 1. ECMWF operational analysis (0.25° resolution) for 1800 UTC on 3 March 2009. (a) Equivalent potential temperature (θ_e, colour shading) on the 500 hPa pressure level, and mean sea level pressure (white contours lines; 3 hPa spacing, 972 hPa minimum contour) . The black cross denotes the location of the CFARR ground site and the dashed line 51.24° latitude. Vertical slices of (b) θ_e and (c) relative humidity are along 51.24° latitude.

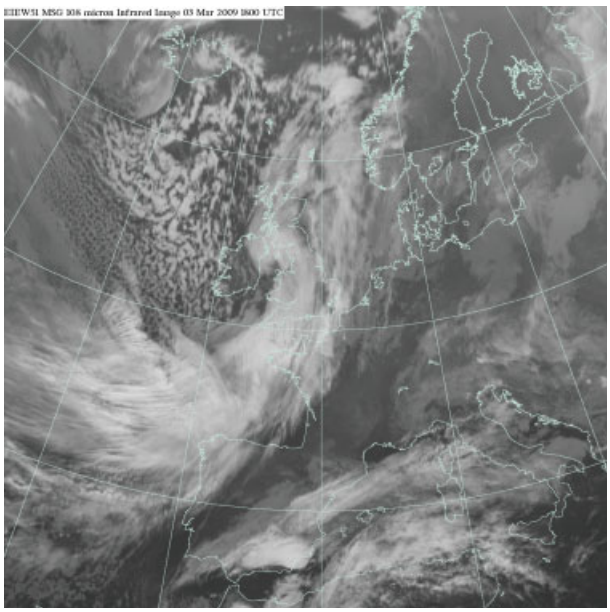

Figure 2. Meteosat second generation (MSG) infrared image (10.8 μm), 1800 UTC on 3 March 2009. This figure is available in colour online at wileyonlinelibrary.com/journal/qj

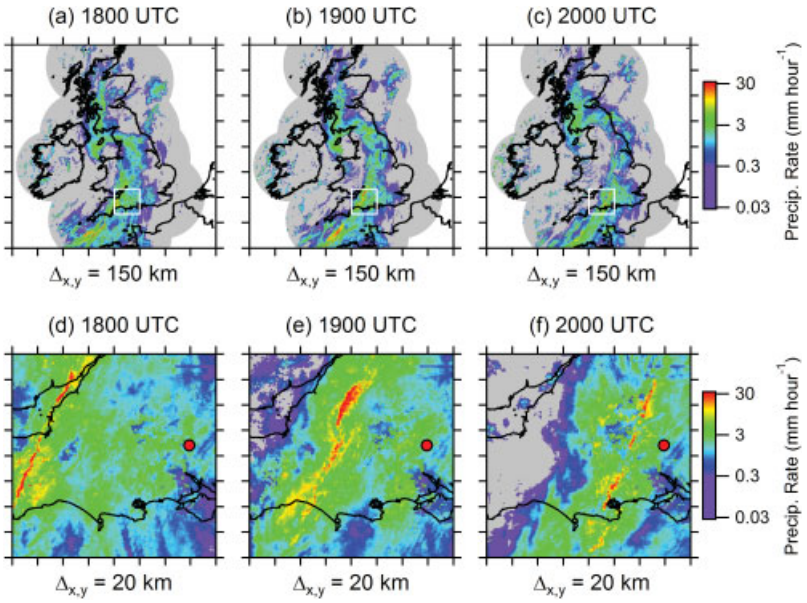

Figure 3. Precipitation rate estimated from UK operational radar network (NIMROD dataset) at (a), (d) 1800 UTC, (b), (e) 1900 UTC and (c), (f) 2000 UTC on 3 March 2009. The domains for (d)–(f) are marked on (a)–(c). Axis ticks on (a)–(c) and (d)–(f) (i.e. $\Delta_{x,y}$) are 150 and 20 km apart respectively. The CFARR ground site is marked in (d)–(f) with a red circle. Minimum detectable rainfall rates are ~ 0.03 mm h^{-1}. Regions within range of the radar network but with no detectable signal are coloured grey.

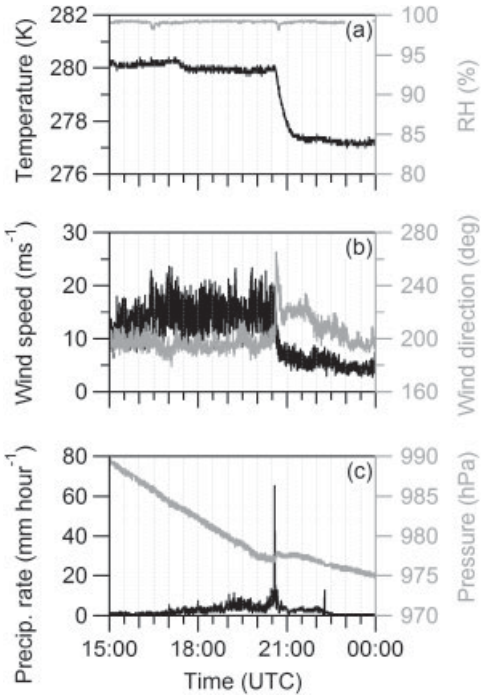

Figure 4. Surface observations from the CFARR ground site of (a) temperature, relative humidity, (b) wind speed, wind direction and (c) precipitation rate and surface pressure.

Figures 3(d)–(f) show precipitation rates in the vicinity of the CFARR ground site. A narrow band of heavy precipitation only a few kilometres wide can be seen to the west of CFARR at 1800 UTC (Figure 3(d)), which moves to the east with time. The detailed structure of the narrow rainband alters as it moves eastward, with some evidence of kinks and gaps at some times and not others. However, the general structure of the rainband (southwest to northeast orientation, precipitation rates, $P > 20$ mm h^{-1}) changes little. This narrow band of heavy precipitation is the NCFR mentioned in previous studies. The NCFR passed over the CFARR ground site (indicated on Figure 3(d)–(f) by a red circle) at $\sim$ 2035 UTC.

Surface observations from CFARR are shown in Figure 4. The passage of the rainband occurs at $\sim$ 2035 UTC, with precipitation rates greater than 60 mm h^{-1} observed for about 1 min using a rapid-response drop-counting raingauge (Norbury and White, 1971). Rapid changes in temperature (-3 °C), wind speed and direction were also observed at approximately the same time. This corresponds with the switch in airmass at the surface from the (relatively) meridional warm sector to the (relatively) zonal cold sector (Figure 4(a)). A characteristic positive jump in the (generally descending) pressure is also seen. Precipitation rates either side of the narrow rainband (in the WCFR) were of the order 1–10 mm h^{-1}. Upon close inspection, it becomes apparent that the NCFR was observed before the changes in wind speed/direction, and the drop in temperature.

3.3. *Rainband microphysics–remote sensing*

Example RHI scans of radar reflectivity factor (dBZ_h, from the horizontal polarisation) and unfolded Doppler velocity (v_u) from CAMRa are shown in Figures 5 and 6. Reported Doppler velocities are positive for motions towards the radar. The scans shown were conducted between 192207 and 192307 UTC and between 200330 and 200400 UTC for Figures 5 and 6 respectively. Both RHIs were obtained along the 255° radial, whilst the BAe-146 aircraft was sampling *in situ* along the same radial. The scan was conducted to the southwest, so the x-axis has been reversed to aid visual interpretation. The detection limit of dBZ_h is -20 at 10 km range, which rises to dB$Z_h = 0$ at 100 km range.

The general features, as shown in Figures 5(a) and 6(a), are low values of reflectivity near cloud top (dB$Z_h < 0$), a bright band (dB$Z_h > 30$) near the melting layer (1–2 km altitude) and typical dBZ_h values of 15–30 at mid-levels. Fallstreaks are present near cloud top (especially in Figure 6(a)), which suggests convective cells are generating ice particles. Cloud top (according to radar reflectivity) varies between 5 and 8 km. Some of the variability in cloud top is a result of the variable detection limit with range, but also due to the fallstreak structure observed. Figure 5(a) shows a bump in the bright band at approximately 57–60 km from CFARR, where the high values of dBZ_h were observed at higher altitudes (up to 2 km) than the surrounding regions. This enhancement in dBZ_h is located above the surface cold front (see below), and indicates the location of the NCFR. This reflectivity feature marking the NCFR is located $\sim$ 25 km from CFARR according to the RHI obtained 40 min later (as shown in Figure 6(a)). Vertical profiles of dBZ_h, extracted from

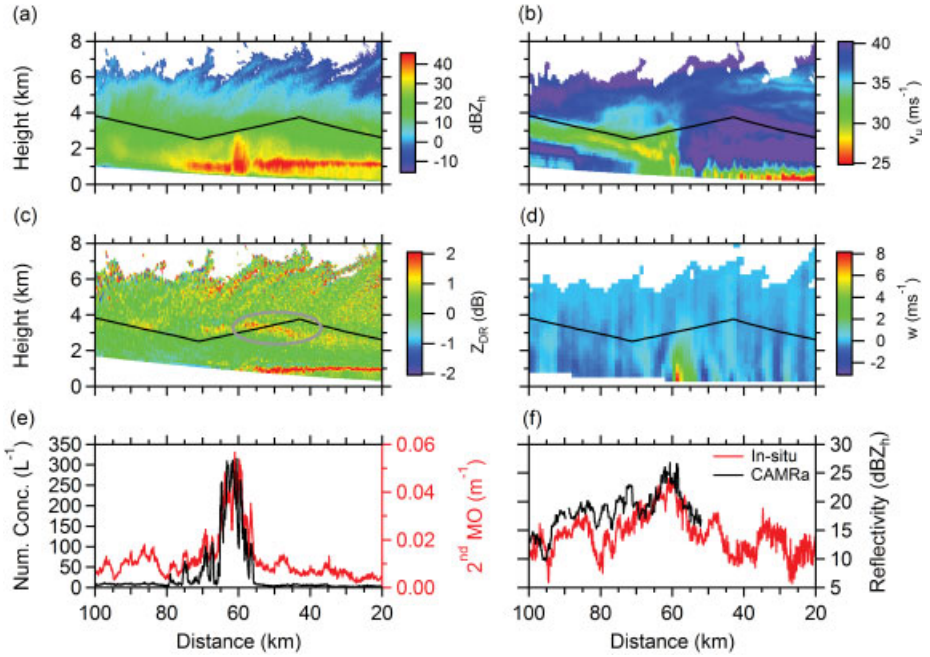

Figure 5. RHI scan of (a) radar reflectivity (dBZ_h), (b) unfolded Doppler velocity (v_u), (c) differential reflectivity (Z_{DR}) and (d) vertical velocity (w) from the 3 GHz radar (CAMRa). The scan was performed between 192207 and 192307 UTC. The radar reflectivity factor was obtained from the horizontally polarised beam. The BAe-146 flight track (190900–192736 UTC) is marked on (a)–(d) with a black line. (e) shows *in situ* number concentrations and the second moment of the PSD (left and right axis respectively) from the merged CIP-15/100 data. (f) shows radar reflectivities obtained along the flight track from CAMRa and that calculated from the *in situ* data. The x-axes are reversed (conventionally showing east to the right, west to the left) as the scan was performed along the 255° radial. Note the detection limit of dB$Z_h = -20$ at 10 km, which rises to dB$Z_h = 0$ at 100 km range. Positive Doppler velocities represent motion towards the radar.

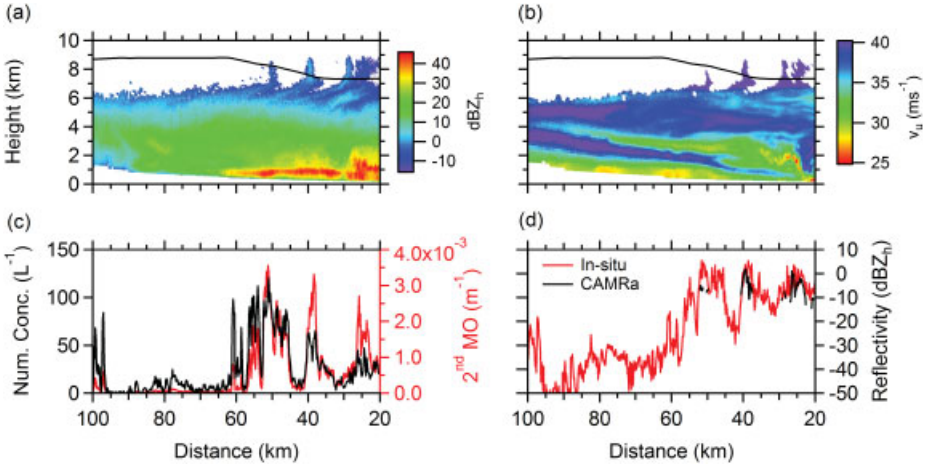

Figure 6. As Figure 5 for (a) and (b), but for the RHI scan spanning the time 200324–200423 UTC, and for flight times 195800–200800 UTC. (c) shows total particle number concentration (left axis) and second moment of size distribution (right axis) *in situ* data. (d) shows measured (CAMRa) and calculated (*in situ* data) radar reflectivty.

the RHI scan in Figure 5(a), are shown in Figure 7(e). The profiles are taken from a distance −10, 0, 10 and 20 km from the centre of the NCFR (positive values being closer to CFARR, downwind of the cold front), and show the impact of both the brightband and NCFR on the dBZ_h structure at lower/mid levels. The dBZ_h structure at upper levels is nearly identical between profiles.

Figure 5(b) shows a large rearward-sloping region of relatively slow-moving targets ($v_u < 35$ ms^{-1}). This large feature represents the location of the boundary between warm and cold air (i.e. slantwise ascent at the cold frontal boundary). The rear-inflow jet which drives the advection/convection is identified by the region of high Doppler velocity ($v_u > 35$ ms^{-1}), located beneath the slanted cold front boundary already mentioned. The smallest values of v_u found in this feature are approx 60 km from CFARR, coincident with the region of elevated dBZ_h (Figure 5(b)) discussed previously.

Other large-scale features which can be seen in the velocity data (Figure 5(b)) include: the low-level jet (LLJ), a region of high wind and low turbulence (as indicated by low Doppler spectral width, not shown) ahead of the cold front (10–50 km distance, 1–4 km altitude), which flows along the length of the front (Jorgensen *et al.*, 2003); and boundary-layer convection ahead of the cold front (10–50 km distance, altitudes less than 1 km), as indicated by low Doppler velocities and increased turbulence. The velocities in this boundary layer are significantly lower than in the LLJ above due to friction at the surface.

The vertical velocity field estimated using the technique described in section 2 is shown in Figure 5(d), indicating a near-vertical line of convection occurring at the surface cold front. The peak updraught velocity (6.9 m s^{-1}) occurs near the surface in association with the cold front and significant updraughts (at least 2 m s^{-1}) extend up to 2 km. Doppler velocities were averaged onto a 1 km (horizontal) by 250 m (vertical) Cartesian grid to derive the vertical wind speeds depicted in Figure 5(d). Vertical velocity calculations made at a finer horizontal resolution (500 m) estimated a more intense updraught associated with the NCFR (peak updraught = 8.2 m s^{-1}). The updraughts in the NCFR below 2 km altitude at 500 m horizontal resolution were 30%

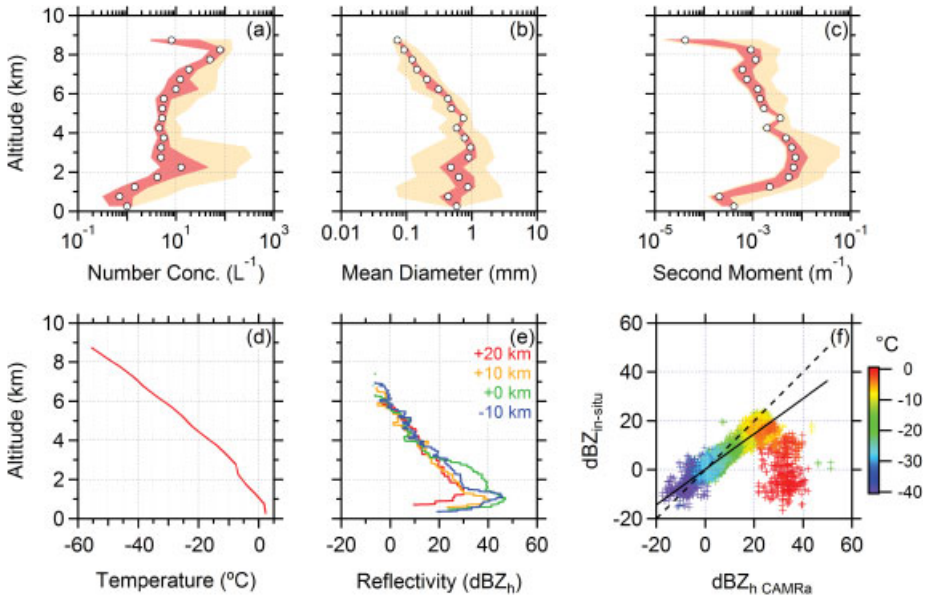

Figure 7. Vertical profile of (a) number concentration, (b) mean diameter, (c) second moment of the PSD and (d) ambient temperature. The merged CIP-15/100 data are used for (a)–(c), and the Rosemount de-iced temperature sensor data for (d). Altitude bins are 500 m wide. Dark shading, light shading and white circles represent interquartile range, 0–25 and 75–100 percentile range, and median values respectively. (e) shows vertical profiles of radar reflectivity at distances of +20, +10, 0 and −10 km relative to the rainband (positive values are closer to CFARR). (f) shows a comparison of measured (from CAMRa) and calculated (from *in situ* data), with datapoints coloured according to ambient temperature.

larger on average than at 1 km resolution. Smaller differences were found at finer resolutions, approaching the range resolution of the radar measurements (300 m).

Also shown in Figure 5 is the Differential Reflectivity (Z_{DR}, Figure 5(c)) from CAMRa. In the bulk of the stratiform cloud above the melting layer the differential reflectivity ($Z_{DR} < 0.5$ dB) is consistent with the presence of irregular aggregates and polycrystals (Wolde and Vali, 2001). However, elevated values of Z_{DR} (1–2 dB) can be seen in two main areas of the RHI scans (Figure 5(c)). First, they can be seen in/around cloud top, specifically in regions where fallstreaks are apparent. This suggests pristine ice particle formation in/around cloud top (Wolde and Vali, 2001; Bailey and Hallett, 2009), in convectively active regions. By pristine ice, we refer to ice particles which have not undergone either aggregation or riming, and so have grown by vapour deposition alone. Note that in these regions Z_{DR} is negatively correlated with dBZ_h. The regions of higher dBZ_h are likely composed of polycrystalline or aggregated ice particles with lower Z_{DR}. The fallstreak structure and anticorrelation between dBZ_h and Z_{DR} suggests that there is some 'sorting' mechanism, perhaps the result of different fall speeds of the two different crystal types. It is worth noting that the Z_{DR} structures could also result from partially rimed/aggregated/sublimated particles.

The second region where high Z_{DR} is observed is a layer at 3–4 km altitude (highlighted by the grey oval in Figure 5(c)), forming a wide inverted U shape, overlying the NCFR. This layer extends for around 30 km in the horizontal, and suggests that some kind of pristine ice particles exist (and are possibly forming) at this level. Subsequent and previous RHI scans show this layer advects towards CFARR with time, with the particles which constitute this layer slowly decending to the surface (at a rate of a few kilometres per hour). Its position extends ahead of the leading edge of the surface cold front, due to wind shear in the vertical. Regions of high differential reflectivity (up to 3 dB) have been observed in regions of embedded convection within frontal cloud, and were associated with pristine columns formed by ice multiplication (Hogan *et al.*, 2002).

The observations presented in Figure 5 fit the conceptual model of a NCFR well (Locatelli *et al.*, 1995; Jorgensen *et al.*, 2003): narrow upright updraught ($w > 7$ m s^{-1}) coinciding with high reflectivities (dB$Z_h > 30$) above the melting layer, both of which are located above a surface cold front.

3.4. *Rainband microphysics–in situ data*

3.4.1. *Bulk in situ properties*

A summary of the *in situ* microphysical properties of the cloud associated with the cold front can be found in Figure 7. The merged CIP-15/100 data from both the NCFR and WCFR are put into 500 m altitude bins for the whole flight. Parameters shown include total number concentration (N_{tot}), mean diameter (D_{mean}), and the second moment of the number concentration distribution (*M2*). We have shown *M2* as it is approximately proportional to the mass concentration according to Locatelli and Hobbs (1974), Brown and Francis (1995) and Heymsfield *et al.*(2007, 2010). These studies related particle mass to diameter using two parameters, *a* and *b*, using the form Mass $= a \times$ Diameter^b. The aforementioned studies have shown that *b* has a value ranging from 1.8 to 2.2). One limitation of using *M2* to represent mass is that it does not take variations in density with particle type into account. Also shown in Figure 7 is the ambient temperature in each altitude bin.

Figure 7(a) shows that large values of particle number concentration are observed at −55°C, near cloud top (median $N_{tot} \sim 60$ L^{-1}, maximum $N_{tot} > 100$ L^{-1}). Note the median concentrations in the highest altitude bin (8.5–9.0 km) are smaller than in the bin below. This is probably due to the ice particles being too small for the imaging probes to detect. Also, cloud top may have varied somewhat during the pass. At lower altitudes, median N_{tot} is significantly lower than these cloud-top concentrations, most likely due to the effects of aggregation and size sorting. An important exception is seen in the 2.0–2.5 km altitude bin ($T = -8$°C), where a second maximum is observed (median $N_{tot} \sim 10$ L^{-1}, maximum $N_{tot} > 100$ L^{-1}). This coincides with the Hallett–Mossop (HM) zone (−3 to −8°C; Hallett and Mossop, 1974) and suggests that ice multiplication is occurring via rime-splinter ejection. Large maximum values of N_{tot} are enhanced in the surrounding altitude bins. This suggests that these secondary ice particles are being transported within the cloud. Images of the ice particles in this region show large numbers of pristine columns (100–400 μm length), which is the main growth habit at these relatively high temperatures. Secondary maxima in ice particle number concentration at approx. −8°C were also observed by Bower *et al.*(1996) in frontal clouds over the UK.

The profile of D_{mean} is shown in Figure 7(b). The smallest particles are found at cloud top ($D_p < 100$ μm), with D_{mean} increasing to ∼1 mm at 4 km altitude. This is largely consistent with the concept of snow formation via aggregation and depositional growth of ice crystals. Significant increases in the variability of D_{mean} (as indicated by the shaded regions) are found at altitudes below 4 km. This is due to the influence of the smaller pristine columns (produced by multiplication in the HM zone) on the size distribution which would otherwise be dominated by larger snow particles. The profile of *M2* shows a general increase with decreasing altitude. An increase in the variability of *M2* can also be seen in the HM zone. *In situ* data shown in Figure 5(e) demonstrate that the region of elevated *M2* is co-located with the region of elevated N_{tot}. Therefore, rime splintering may be contributing to the observed increase in *M2* (and thus the mass concentration). It should be noted that there were no instruments on board the aircraft capable of phase discrimination of particles with $D_p < 50$ μm. These could have had a significant effect on the N_{tot} and D_{mean} profiles in Figure 7.

In situ data from a subset of the flight are shown in Figure 5(e) and (f). The aircraft position during the period shown (190900–192736 UTC) is indicated by the black line in Figure 5(a)–(d), and coincides with the radar scan (192207–192307 UTC). The aircraft track skims the top of the high reflectivity/Doppler feature identified earlier as the NCFR. In this region a clear increase in the number concentration is observed (from $N_{tot} < 10$ L^{-1} to $N_{tot} > 100$ L^{-1}), and pristine columns presumably generated by HM multiplication tend to dominate. A corresponding increase in *M2* (proportional to mass concentration) is also clearly apparent. Therefore, the HM multiplication process appears to be highly active in the NCFR, at least in terms of affecting number concentrations. The increase in *M2* is partly related to the large number of particles from HM multiplication, as will be discussed in section 3.4.2.

Comparisons of the measured radar reflectivity (from the CAMRa data, extracted along the aircraft flight track), with that calculated using the *in situ* data, are shown in Figures 5(f) and 6(d). We have used the method outlined by Hogan *et al.*(2006) to perform the calculation of reflectivity from *in situ* data, using the mass–diameter relationship of Brown and Francis (1995). The reflectivity data from measurement and calculation agree to within 5–7 dB*Z* and show similar peaks/troughs in the data. The discrepancies can be accounted for in deviations from the mass– diameter relationship used, due to the dependency of radar reflectivity the square of the mass. A comparison of the measured and calculated radar reflectivity for the entire flight is shown in Figure 7(f). When ignoring the reflectivity values which are enhanced due to the brightband at 0 °C, the data compare very well ($R^2 = 0.83$), albeit with deviations from a 1 : 1 correlation (slope = 0.73).

During the aircraft pass shown in Figure 5, only minimal amounts of liquid water were detected (< 0.1 g m^{-3}). This may seem low considering the convective activity, but the aircraft passed over (and not within) the main reflectivity/convective feature. Therefore, updraughts in the region sampled may have been significantly lower than those in the updraught core. This could explain the depletion of liquid water, as the Wegener–Bergeron–Findeisen process would be active in the region sampled, because of the reduced availability of water vapour in the updraught and the presence of a large number of newly formed ice particles. No measurements of vertical wind speed are available from the BAe-146 due to instrument icing problems at this time. CFARR data (discussed earlier) suggest peak updraughts were less than 0.5 m s^{-1} during the pass by the aircraft. Based on the framework outlined by Korolev and Mazin (2003), the estimated minimum vertical velocity required to maintain supercooled cloud droplets given the measured ice particle population is of order 1 m s^{-1}. There are no passes through the region of greatest reflectivity within the NCFR by the BAe-146.

In situ data obtained from a subsequent run at altitudes of 7–9 km are shown in Figure 6(c)–(d). Large regions of this RHI scan show no detectable radar return despite *in situ* data confirming the presence of cloud ice particles in the same region. However, the calculated reflectivity from these regions is below the detection limit of the CAMRa. The RHI scan (Figure 6(a)) shows several isolated features protruding from the otherwise uniform cloud top. Ice particle number and mass (*M2*) concentrations are found to be much higher in this region. This suggests some form of convective activity enhancing nucleation when compared to the rather stable surrounding regions.

3.4.2. *Particle size distributions*

The changes of the particle size distribution with altitude are shown in Figure 8. These spectra (approx. 5 min averages) are taken from periods where the BAe-146 was flying at constant altitude along the 255° radial. Also shown on Figure 8 are cumulative distribution frequency (CDF) curves for the number

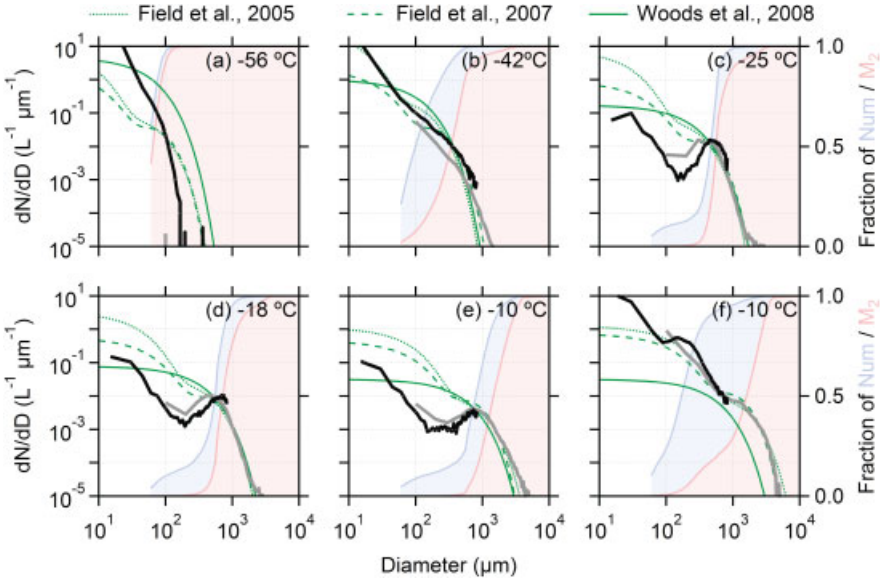

Figure 8. Size distributions of number concentration from the CIP-15 (black) and CIP-100 (grey) on board the BAe-146 at the indicated temperatures. Also shown in green are curves using parametrizations of the size distribution. Cumulative Distribution Frequency (CDF) curves for the number concentration (blue) and second moment (red) are plotted on the right axis as a function of increasing particle diameter (D_p). Panel represent ambient temperatures of (a) −56°C, (b) −42°C, (c) −25°C, (d) −18°C, (e) and (f) −10°C. (e) and (f) were obtained away from and near to the NCFR respectively.

concentration and second moment (*M2*), to provide an indication of which parts of the size distribution contribute to the total number concentration and *M2* (or mass) respectively. These CDF curves are generated from the merged CIP-15/100 particle size distributions, and do not include the smallest particles ($D_p <$ 60 μm) in order to exclude cloud droplets from the analysis. This conforms to the recommendations of Korolev (2007), which state that images obtained with OAPs (Optical Array Probes, such as the CIP and 2D-S) which are less than three to four pixels wide should be ignored due to the digitization/depth of field uncertainties.

The spectra from near cloud top (e.g. Figure 8(a) and (b)) are narrow and unimodal. Images show these particles are pristine bullet-rosette type ice crystals. Lower down in the cloud (Figure 8(c)–(e)), a second mode forms at larger sizes ($D_p >$ 300 μm), similar to that observed by Field (2000). These particles are more complex and aggregation appears to be important in forming these snow particles. The size distributions shown in Figure 8(e) and (f) are obtained at the same altitude/temperature, but are from outside and inside the region of high ice crystal concentration observed near the NCFR respectively. The spectrum obtained near the NCFR shows the large increase in particle number at smaller sizes ($D_p <$ 1 mm), which are the HM secondary particles. Inspection of the imagery data reveals these small particles are dominated by ice particles, specifically columns.

The CDF curves in Figure 8(f) show that the contribution of particles with $D_p <$ 400 μm is approximately 15% and 90% for *M2* and number concentration respectively. The corresponding values for Figure 8(e), (which was at the same altitude/temperature, but further away from the NCFR), are 3% and < 10% for *M2* and number concentration respectively. This shows a significant increase in the relative contribution to *M2* (and thus mass) of the < 400 μm particles (which are mostly a result of the HM multiplication) in the NCFR.

A number of other studies in midlatitude stratiform precipitation have derived parametrizations to fit the particle size distributions observed over many case-studies. We have included these data in Figure 8, based on the parametrizations of Field *et al.*(2005, 2007) and Woods *et al.*(2008)(referred to as F05, F07 and W08 respectively). The F05 and F07 studies used identical approaches, invoking a 'universal size distribution' which is scaled according to the second and third moments of the size distribution. The second moment is an input, and the third moment is predicted using a temperature-dependent parametrization. The universal size distribution contains three unique parameters which define its shape, and allows the representation of relatively complex size distributions. The W08 study used a temperature-dependent parametrization to derive a two-parameter negative exponential size distribution.

The agreement between the measured and parameterized size distributions is generally good for $D_p >$ 1000 μm. Exceptions to this include Figure 8(a) (−56°C), where the comparison is not valid due to the lack of large particles, and Figure 8(f)(−10°C in the NCFR region), where W08 underestimates the large particle concentration by an order of magnitude. Below 1000 μm, most of the parametrizations overpredict the number concentration by between one and two orders of magnitude. Exceptions to this can be seen in Figure 8(b) (−42°C) and 8(f) (−10°C in the NCFR region), where the agreement is within one order of magnitude. The quality of agreement between the measurements and parametrizations could be due to a number of reasons, including natural variability between cloud systems. However, what is clear is that the parametrizations available do not delineate between regions which are at the same temperature, but which are and are not influenced by the HM process. Therefore the accuracy of the parametrizations used to represent the PSD is likely to be compromised in (or near to) regions where the HM process is active (or inactive), such as the NCFR in this study. The level of over/underprediction is dependent on the level of influence of the HM process on the dataset used to derive the parametrizations.

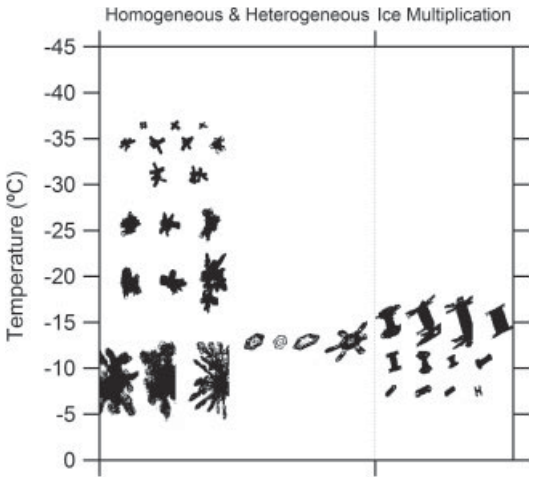

Figure 9. Example particle images from the 2D-S probe as observed in the different temperature/process regions of the cloud.

3.4.3. *Particle imagery*

A summary of the particle habits observed at different altitudes/temperatures over all runs is shown in Figure 9. The images shown here are typical of those found at any given temperature. However, a large amount of variability is observed at any one time, especially when imaging small particles like bullet-rosettes near cloud top, and columns near the NCFR, and also aggregate particles.

Figure 9 reveals several interesting features. First of all, bullet-rosette particles are detected near cloud top. This is the dominant growth regime at low (< −30°C) temperatures (Bailey and Hallett, 2009). The fallstreaks observed near cloud top (Figure 6(a)) suggest convection is driving nucleation by increasing the relative humidity and reducing cloud-top temperatures (whilst increasing cloud-top height). Also low cloud-top temperatures (−55°C) lend weight to the idea of homogeneous nucleation being responsible for some of the observed ice formation. However, heterogeneous nucleation can also be enhanced in such convective features, and we have no method to separate the action of each mechanism.

Secondly, low concentrations of relatively small (< 800 μm) pristine stellar plates and hexagonal plates are observed at temperatures lower than −12°C. This suggests that heterogeneous nucleation is occurring within the stratiform cloud region (Bailey and Hallett, 2009) since, if they were formed via homogeneous nucleation, they would have grown to larger sizes (via aggregation and/or deposition), and would most likely have a more complex crystal shape. We are unable to determine the extent to which heterogeneous nucleation is occurring as it requires an accurate image classification scheme, which we do not have at present. As already mentioned, large numbers of column ice particles are observed near the NCFR.

Figure 9 also shows that near the NCFR, but at slightly lower temperatures (approx. −12°C), capped columns are observed. We argue that these are columns which have formed in the HM region and have been transported vertically upwards in the updraught. As they are lifted above the −8°C level, they enter an environment favouring plate-like growth (Bailey and Hallett, 2009). This leads to the formation of plates on the ends of the columns. These capped-columns are found in the region of high Z_{DR} identified by CAMRa; this region had a horizontal extent of ∼ 30 km horizontal extent and a vertical thickness of only a few hundred metres. It appears this high Z_{DR}/capped-column region is some form of outflow from the top of the NCFR (analogous to anvil cirrus in regions of deep convection, albeit embedded within stratiform cloud). Based on the Z_{DR} data shown in Figure 5(e), this layer appears to advect faster than the NCFR itself, likely due to wind shear in the vertical.

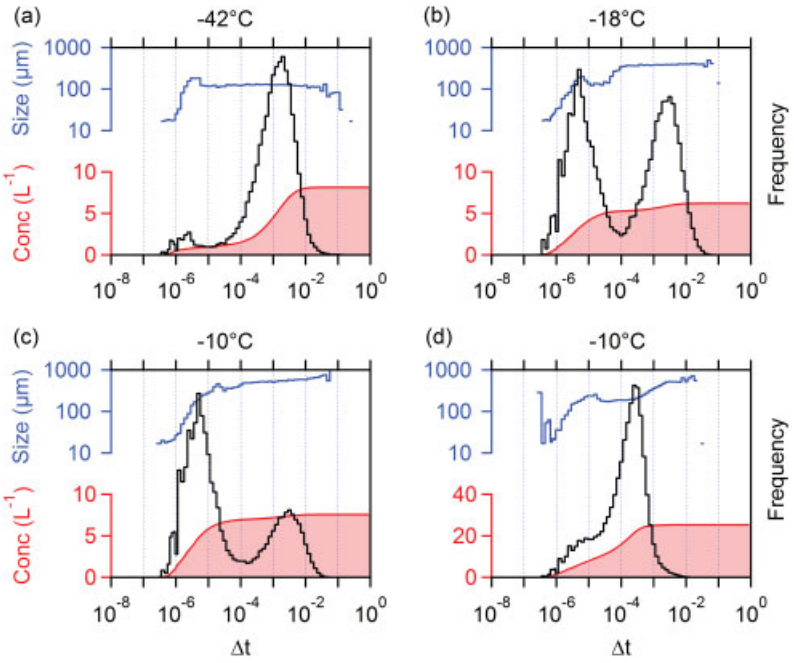

Figure 10. Particle inter-arrival time histograms (black, right axis) for the CIP-15 at (a) −42°C, (b) −18°C and from (c) within and (d) outside the NCFR regions at −1°C. Also shown are the mean area equivalent diameter (blue) and the cumulative distribution function (CDF) of the number concentration (red).

Wolde and Vali (2001) show that regions of capped columns mixed with pristine plates do result in a detectable signal in Z_{DR} (∼1.5) at near-horizontal beam angles. This signal in Z_{DR} is small in comparison to that for pristine plates alone (∼6). There are no measurements available in the literature of Z_{DR} for isolated pristine capped columns.

3.4.4. *Probe inter-arrival time analysis*

In order to remove shattering artefacts from the CIP-15 and CIP-100 probes, histograms of particle IAT were examined. Examples are shown in Figures 10 and 11 for the CIP-15 and CIP-100 respectively. These histograms were constructed for the same time periods as the size distributions in Figure 8. IAT histograms are not shown for −56 and −25°C as they largely replicate those for −42°C. Also shown in Figures 10 and 11 are mean particle size in each IAT bin (using the area equivalent diameter), and the CDF of the number concentration. These are added to provide an indication of the typical size of particle in each IAT mode/bin, and the relative contribution of each mode in the IAT histogram to the total number concentration.

The CIP-15 generally shows bimodal spectra with a shattering mode to the left, centred just below 1×10^{-5} s, and another mode of particles to the right. The right-hand mode located at $\sim 2 \times 10^{-3}$s in Figure 10(a–c) represents intact (i.e. non-shattering) particles and does not generally extend below 10^{-4}s, making this a suitable choice as an IAT threshold in these regions. The shattered particles below the IAT threshold can contribute significantly to the number concentration (e.g. >80% at −18°C as in Figure 10(b)), and so must be removed to avoid contamination. This strict thresholding method may remove a small number of valid particles, but the IAT histograms show these erroneously filtered particles only have a small contribution to the total number concentration.

Figure 10(d) is from the NCFR where HM multiplication is acting to increase the ambient ice particle concentration. The large concentrations observed here cause a shift in the mode of the valid particles to the left, centred at $\sim 2 \times 10^{-4}$ s. Due to this shift and the width of the mode, a large number of valid particles are pushed below the previously acceptable IAT threshold of 10^{-4} s. A threshold of 10^{-5} s is more appropriate in this region. Note that the relative number of intact particles greatly exceeds the shattered ones in the HM multiplication zone, and near cloud top.

The CIP-100 shows modest signs of bi-modality (and hence shattering) at the lower temperatures (Figure 11(a) and (b)). At these levels, particles with an IAT $< 10^{-4}$ s contribute around 15% to the total number concentration measured. However, Figure 10(c) shows a more pronounced shattering mode, with contaminations of approximately 50% to the number concentration with an IAT $< 10^{-4}$ s. In the NCFR where HM multiplication was observed (Figure 11(d)), the shattering mode is engulfed by valid particle counts. This is due to a shift to the left as the ambient particle concentration increases by over an order of magnitude relative to the region shown in Figure 11(c). Using an IAT threshold of 10^{-4} s in the NCFR region leads to the reduction of the number concentration by 90%, when most of these particles are valid. A more modest IAT threshold of 10^{-5} s in this region results in a loss of only 10% of the particles.

In order to take into account this variability in the IAT threshold, a preliminary stage of data processing was conducted with an IAT threshold of 10^{-4} s. As discussed above, this is at times too large and will lead to a negative bias in the reported concentrations (especially for the CIP-100 in the HM zone). After the preliminary processing, periods identified to have high number concentrations (> 20 L^{-1}) were reprocessed with a new IAT of 10^{-5} s to reduce this negative bias. The result of this was a significant improvement between the CIP-15 and CIP-100 in the overlap region, by allowing more counts in the lower size bins of the CIP-100 in the HM zone. The agreement between the probes in the other regions of the cloud was unaltered by this modified IAT threshold. This IAT filtering was implemented for all the analysis shown in this article. It should be noted that using IAT filtering on OAP may not remove all shattering artefacts (Korolev *et al.*, 2011), and so some shattering artefacts may still be present.

The influence of shattering artefacts on other published datasets needs to be understood. Particle IAT analyses should be conducted on key datasets when particle time stamp information is available. When this information is not available, data below a certain size (nominally 300 μm) should be discarded. The shattering characteristics for different probes need to be understood. Shattering artefacts should be minimised before they affect data, instead of relying on post-processing techniques. Therefore, using modified probe tips as described by Korolev *et al.*(2011, 2012) is highly recommended.

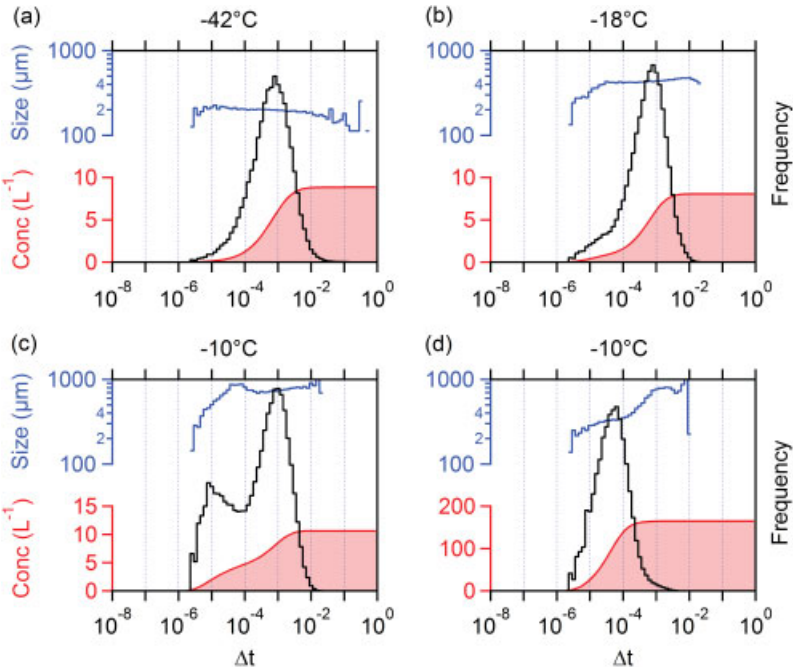

Figure 11. As Figure 10, but for the CIP-100.

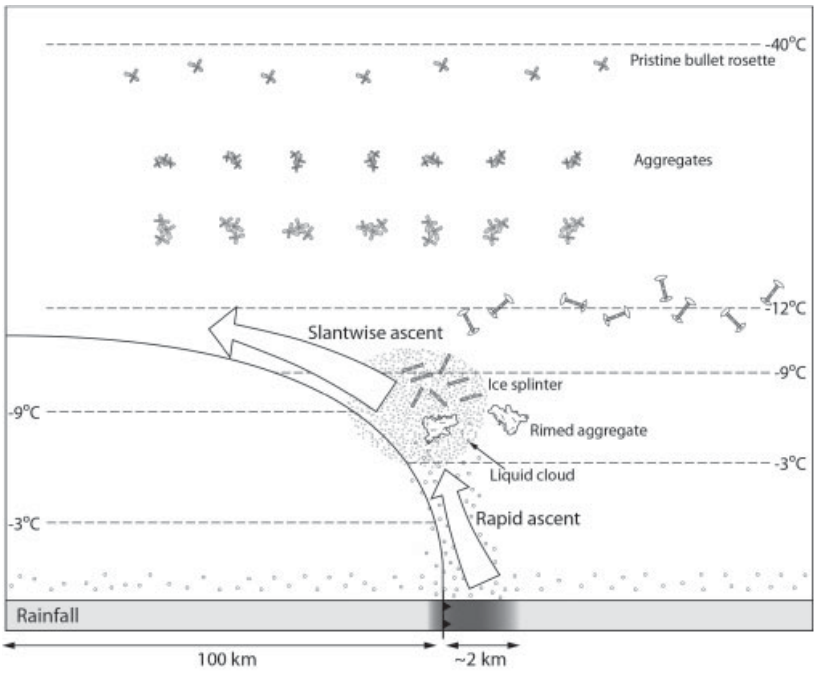

Figure 12. Schematic of microphysical processes controlling ice number concentration and precipitation formation in a narrow cold frontal rainband.

3.5. Summary of the NCFR

Ice multiplication appears to be active in the NCFR as it has all the necessary requirements. Convection is driven from near the surface due to the movement and strength of the cold front. Significant amounts of supercooled liquid water are generated as a result. We also have stratiform precipitation/snow from the larger-scale slantwise ascent of the system as a whole, as well as that produced at cloud top in convectively generated fallstreaks. Combining the liquid water source and the stratiform precipitation with favourable thermodynamic conditions (i.e. suitable cloud-base temperature) leads to a scenario where the HM process is highly active. We have attempted to visualise this scenario in Figure 12. The splinters produced can either aggregate/rime and precipitate out of the rainband, or are transported vertically upwards into an outflow region and develop into capped columns.

4. Conclusions

We have presented *in situ* and remote-sensing measurements in a cold frontal system. The system was found to contain a Narrow Cold Frontal Rainband (NCFR), embedded within a Wide Cold Frontal Rainband (WCFR). Our conclusions are:

- The effects of ice multiplication were observed in the vicinity of the NCFR, resulting in the highest ice particle number concentrations being observed at temperatures $> -10^{\circ}$C. This was most likely due to the rime splintering process as described by Hallett and Mossop (1974). Evidence supporting this lies in the ice particle number concentrations (> 100 L^{-1}), particle sizes (~ 400 μm), particle habit (pristine columns), and location (proximity to the NCFR and the -3 to -8°C isotherms).

- Ice multiplication occurred due to the generation of supercooled liquid water along the convective NCFR. The convection spanned the region where rime splintering is known to be active (−3 to −8°C). Snow particles from the stratiform region appear to be rimed near the NCFR, with no evidence of graupel. This suggests that rime splintering results from the interaction of the NCFR and stratiform precipitation (and not graupel), and that snow particles are acting as sites for rime splintering. This was also shown by Marwitz (1987). We cannot rule out the presence of graupel in regions we did not sample, such as in the regions of peak radar reflectivity.
- Particles generated via multiplication accounted for a significant fraction of the ice water content (∼ 15%). These particles will precipitate slowly due to their small size, altering the precipitation budget of the system and the pattern of latent heat release.
- Some ice particles resulting from the multiplication process were transported out of the convective feature by the updraught, forming an elevated layer of ice crystals. These particles had entered a new growth regime, and evolved from pristine columns into capped columns. This elevated layer from the convective outflow was identifiable in the radar differential reflectivity data.
- Available parametrizations which diagnose the cloud particle size distribution do not represent the effects of rime splintering. Most parametrizations are functions of temperature alone. More sophisticated parametrizations use multiple parameters, but still do not include the effects of ice multiplication.
- The presence of secondary ice and mixed-phase conditions requires modifications to artefact removal from imaging probes when considering particle IAT analysis. This has impacts on both medium- (e.g. CIP-15) and coarse- (e.g. CIP-100) resolution imaging probes. The use of anti-shatter tips on imaging probes, as described by Korolev *et al.*(2011), reduces these complications and is recommended, as IAT analysis has shown to be less effective at removing artefacts than modified probe designs.
- The majority of primary ice particles were generated close to cloud top by homogeneous and heterogeneous nucleation. These were often associated with convective elements identified by the radar and led to fall streaks of growing and aggregating ice crystals.
- The relative role of homogeneous and heterogeneous ice nucleation on the formation of the stratiform precipitation cannot be quantified, but it is likely that homogeneous nucleation is occurring at temperatures below −35°C, and heterogeneous nucleation throughout the depth of the cloud.
- Model studies are required to quantify the roles of homogeneous, heterogeneous and secondary ice formation mechanisms on precipitation formation in NCFRs in a variety of conditions (dynamical, thermodynamical, and microphysical). The feedback on dynamics via alterations to latent heating patterns should also be explored.

Acknowledgements

This work was funded by the NERC APPRAISE programme, grant number NE/E01125X/1. We would like to acknowledge the support from FGAM, FAAM and Direct Flight in obtaining the aircraft dataset. We would also like to thank the following for supporting the CFARR measurements: Andrew Barrett (University of Reading), Darcy Ladd and Charles Wrench (CFARR). Operational analysis fields were obtained from the ECMWF data archive (http://data.ecmwf.int/data/). We would like to acknowledge the UK Met Office for the CIP-100 data. The Meteosat image and operational radar data were obtained from the British Atmospheric Data Centre (BADC) online archive.

References

Agusti-Panareda A, Gray SL, Belcher SE. 2009. On the dependence of boundary-layer ventilation on frontal type. *J. Geophys. Res.* **114**: D05305, DOI: 10.1029/2008JD010694.

Bailey MP, Hallett J. 2009. A comprehensive habit diagram for atmospheric ice crystals: confirmation from the laboratory, AIRS II, and other field studies. *J. Atmos. Sci.* **66**: 2888–2899, DOI: 10.1175/2009JAS2883.1.

Baumgardner D, Jonsson H, Dawson W, O'Connor D, Newton R. 2001. The cloud, aerosol and precipitation spectrometer: a new instrument for cloud investigations. *Atmos. Res.* **59**: 251–264, DOI: 10.1016/S0169-8095(01)00119-3.

Bower KN, Moss SJ, Johnson DW, Choularton TW, Latham J, Brown PRA, Blyth AM, Cardwell J. 1996. A parametrization of the ice water content observed in frontal and convective clouds. *Q. J. R. Meteorol. Soc.* **122**: 1815–1844, DOI: 10.1002/qj.49712253605.

Brown PRA, Francis PN. 1995. Improved measurements of the ice water content in cirrus using a total-water probe. *J. Atmos. Oceanic Technol.* **12**: 410–414, DOI: 10.1175/1520-0426(1995)012<0410:IMOTIW>2.0.CO;2.

Browning KA. 1986. Conceptual models of precipitation systems. *Weather and Forecasting* **1**: 23–41, DOI: 10.1175/1520-0434(1986)001<0023:CMOPS>2.0.CO;2.

Browning KA, Reynolds R. 1994. Diagnostic study of a narrow cold-frontal rainband and severe winds associated with a stratospheric intrusion. *Q. J. R. Meteorol. Soc.* **120**: 235–257, DOI: 10.1002/qj.49712051602.

Browning KA, Roberts NM. 1996. Variation of frontal and precipitation structure along a cold front. *Q. J. R. Meteorol. Soc.* **122**: 1845–1872, DOI: 10.1002/qj.49712253606.

Chapman D, Browning KA. 1998. Use of wind-shear displays for Doppler radar data. *Bull. Am. Meteorol. Soc.* **79**: 2685–2691.

Crawford I, Bower KN, Choularton TW, Dearden C, Crosier J, Westbrook C, Capes G, Coe H, Connolly PJ, Dorsey JR, Gallagher MW, Williams P, Trembath J, Cui Z, Blyth AM. 2012. Ice formation and development in aged, wintertime cumulus over the UK: observations and modelling. *Atmos. Chem. Phys.* **12**: 4963–4985, DOI: 10.5194/acp-12-4963-2012.

Crosier J, Bower KN, Choularton TW, Westbrook CD, Connolly PJ, Cui ZQ, Crawford IP, Capes GL, Coe H, Dorsey JR, Williams PI, Illingworth AJ, Gallagher MW, Blyth AM. 2011. Observations of ice multiplication in a weakly convective cell embedded in supercooled mid-level stratus. *Atmos. Chem. Phys.* **11**: 257–273, DOI: 10.5194/acp-11-257-2011.

Cui Z, Blyth AM, Bower KN, Crosier J, Choularton T. 2012. Aircraft measurements of wave clouds. *Atmos. Chem. Phys.* **12**: 9881–9892, DOI: 10.5194/acp-12-9881-2012.

Field PR. 2000. Bimodal ice spectra in frontal clouds. *Q. J. R. Meteorol. Soc.* **126**: 379–392, DOI: 10.1002/qj.49712656302.

Field PR, Hogan RJ, Brown PRA, Illingworth AJ, Choularton TW, Cotton RJ. 2005. Parametrization of ice-particle size distributions for mid-latitude stratiform cloud. *Q. J. R. Meteorol. Soc.* **131**: 1997–2017, DOI: 10.1256/qj.04.134.

Field PR, Heymsfield AJ, Bansemer A. 2006. Shattering and particle interarrival times measured by optical array probes in ice clouds. *J. Atmos. Oceanic Technol.* **23**: 1357–1371, DOI: 10.1175/JTECH1922.1.

Field PR, Heymsfield AJ, Bansemer A. 2007. Snow size distribution parameterization for midlatitude and tropical ice clouds. *J. Atmos. Sci.* **64**: 4346–4365, DOI: 10.1175/2007JAS2344.1.

Goddard JWF, Eastment JD, Tan J. 1994. 'Self-consistent measurements of differential phase and differential reflectivity in rain'. In preprints forøth*International Geoscience and Remote Sensing Symposium, 1994. IGARSS '94. Surface and Atmospheric Remote Sensing: Technologies, Data Analysis and Interpretation*, Vol. 1. 369–371, Pasadena, CA, DOI: 10.1109/IGARSS.1994.399128.

Hallett J, Mossop SC. 1974. Production of secondary ice particles during the riming process. *Nature* **249**: 26–28, DOI: 10.1038/249026a0.

Heymsfield AJ, Parrish JL. 1978. A computational technique for increasing the effective sampling volume of the PMS two-dimensional particle size spectrometer. *J. Appl. Meteorol.* **17**: 1566–1572, DOI: 10.1175/1520-0450(1978)017<1566:ACTFIT>2.0.CO;2.

Heymsfield AJ, Bansemer A, Twohy CH. 2007. Refinements to ice particle mass dimensional and terminal velocity relationships for ice clouds. Part I: temperature dependence. *J. Atmos. Sci.* **64**: 1047–1067, DOI: 10.1175/JAS3890.1.

Heymsfield AJ, Schmitt C, Bansemer A, Twohy CH. 2010. Improved representation of ice particle masses based on observations in natural clouds. *J. Atmos. Sci.* **67**: 3303–3318, DOI: 10.1175/2010JAS3507.1.

Hobbs PV, Persson POG. 1982. The mesoscale and microscale structure and organization of clouds and precipitation in midlatitude cyclones. Part V: the substructure of narrow cold-frontal rainbands. *J. Atmos. Sci.* **39**: 280–295, DOI: 10.1175/1520-0469(1982)039<0280:TMAMSA>2.0.CO;2.

Hogan RJ, Field PR, Illingworth AJ, Cotton RJ, Choularton TW. 2002. Properties of embedded convection in warm-frontal mixed-phase cloud from aircraft and polarimetric radar. *Q. J. R. Meteorol. Soc.* **128**: 451–476, DOI: 10.1256/003590002321042054.

Hogan RJ, Mittermaier MP, Illingworth AJ. 2006. The retrieval of ice water content from radar reflectivity factor and temperature and its use in evaluating a mesoscale model. *J. Appl. Meteorol. Climatol.* **45**: 301–317, DOI: 10.1175/JAM2340.1.

James PK, Browning KA. 1979. Mesoscale structure of line convection at surface cold fronts. *Q. J. R. Meteorol. Soc.* **105**: 371–382, DOI: 10.1002/qj.49710544404.

Jorgensen DP, Pu Z, Persson POG, Tao W-K. 2003Variations. associated with cores and gaps of a pacific narrow cold frontal rainband. *Mon. Weather Rev.* **131**: 2705–2729, DOI: 10.1175/1520-0493(2003)131<2705:VAWCAG>2.0.CO;2.

Korolev A. 2007. Reconstruction of the sizes of spherical particles from their shadow images. Part I: theoretical considerations. *J. Atmos. Oceanic Technol.* **24**: 376–389, DOI: 10.1175/JTECH1980.1.

Korolev AV, Mazin IP. 2003. Supersaturation of water vapor in clouds. *J. Atmos. Sci.* **60**: 2957–2974, DOI: 10.1175/1520-0469 (2003)060<2957:SOWVIC>2.0.CO;2.

Korolev AV, Emery EF, Strapp JW, Cober SG, Isaac GA, Wasey M, Marcotte D. 2011. Small ice particles in tropospheric clouds: fact or artifact? Airborne icing instrumentation evaluation experiment. *Bull. Am. Meteorol. Soc.* **92**: 967–973, DOI: 10.1175/2010BAMS3141.1.

Korolev A, Emery E, Creelman K. 2012. Modification and tests of particle probe tips to mitigate effects of ice shattering. *J. Atmos. Oceanic Technol.* **30**: 690–708, DOI: 10.1175/JTECH-D-12-00142.1.

Lance S, Brock CA, Rogers D, Gordon JA. 2010. Water droplet calibration of the Cloud Droplet Probe (CDP) and in-flight performance in liquid, ice and mixed-phase clouds during ARCPAC. *Atmos. Meas. Tech.* **3**: 1683–1706, DOI: 10.5194/amt-3-1683-2010.

Lawson RP, O'Connor D, Zmarzly P, Weaver K, Baker B, Mo Q, Jonsson H. 2006. The 2D-S (Stereo) probe: design and preliminary tests of a new airborne, high-speed, high-resolution particle imaging probe. *J. Atmos. Oceanic Technol.* **23**: 1462–1477, DOI: 10.1175/JTECH1927.1.

Locatelli JD, Hobbs PV. 1974. Fall speeds and masses of solid precipitation particles. *J. Geophys. Res.* **79**: 2185–2197, DOI: 10.1029/JC079i015p02185.

Locatelli JD, Martin JE, Hobbs PV. 1995. Development and propagation of precipitation cores on cold fronts. *Atmos. Res.* **38**: 177–206. http://www.sciencedirect.com/science/article/pii/016980959400093S.

Marwitz JD. 1987. Deep orographic storms over the Sierra Nevada. Part II: the precipitation processes. *J. Atmos. Sci.* **44**: 174–185, DOI: 10.1175/1520-0469(1987)044<0174:DOSOTS>2.0.CO;2.

Matejka TJ, Houze RA, Hobbs PV. 1980. Microphysics and dynamics of clouds associated with mesoscale rainbands in extratropical cyclones. *Q. J. R. Meteorol. Soc.* **106**: 29–56, DOI: 10.1002/qj.49710644704.

Norbury JR, White WJ. 1971. A rapid-response rain gauge. *J. Phys. E: Sci. Instrum.* **4**: 601–602.

Rutledge SA, Hobbs PV. 1984. The mesoscale and microscale structure and organization of clouds and precipitation in midlatitude cyclones. XII: a diagnostic modeling study of precipitation development in narrow cold-frontal rainbands. *J. Atmos. Sci.* **41**: 2949–2972, DOI: 10.1175/1520-0469(1984)041<2949:TMAMSA>2.0.CO;2.

Stoelinga MT, Hobbs PV, Mass CF, Locatelli JD, Colle BA, Houze RA, Rangno AL, Bond NA, Smull BF, Rasmussen RM, Thompson G, Colman BR. 2003. Improvement of microphysical parameterization through observational verification experiment. *Bull. Am. Meteorol. Soc.* **84**: 1807–1826, DOI: 10.1175/BAMS-84-12-1807.

Westbrook CD, Illingworth AJ. 2011. Evidence that ice forms primarily in supercooled liquid clouds at temperatures> -27°C. *Geophys. Res. Lett.* **38**: L14808, DOI: 10.1029/2011GL048021.

Wolde M, Vali G. 2001. Polarimetric signatures from ice crystals observed at 95 GHz in winter clouds. Part I: dependence on crystal form. *J. Atmos. Sci.* **58**: 828–841, DOI: 10.1175/1520-0469(2001)058<0828:PSFICO>2.0.CO;2.

Woods CP, Stoelinga MT, Locatelli JD. 2008. size spectra of snow particles measured in wintertime precipitation in the Pacific Northwest. *J. Atmos. Sci.* **65**: 189–205, DOI: 10.1175/2007JAS2243.1.